Fractionalization in Fractional Correlated Insulating States at $n \pm 1/3$ filled twisted bilayer graphene

Dan Mao,[1] Kevin Zhang,[1] and Eun-Ah Kim[1, 2, 3, 4]

[1] *Laboratory of Atomic and Solid State Physics, Cornell University, 142 Sciences Drive, Ithaca NY 14853-2501, USA*
[2] *Radcliffe Institute for Advanced Study at Harvard, Harvard University, 10 Garden Street, Cambridge MA 02138, USA*
[3] *Department of Physics, Harvard University, 17 Oxford Street, Cambridge MA 02138, USA*
[4] *Department of Physics, Ewha Womans University*

(Dated: October 2021)

Fractionalization without time-reversal symmetry breaking is a long sought-after goal that manifests non-trivial correlation effects. While exactly solvable models offered many new theoretical insights, the physical realization of time-reversal symmetric fractionalization remained out of reach. The earlier proposal of correlated insulating states at $n \pm 1/3$ filling in twisted bilayer graphene and recent experimental observations of insulating states at those fillings stongly suggest that moiré graphene systems provide a new platform to realize time-reversal symmetric fractionalized states. However, the nature of fractional excitations and the effect of quantum fluctuation on the fractional correlated insulating states are unknown. We show that excitations of the fractional correlated insulator phases in the strong coupling limit carry fractional charges and exhibit fractonic restricted mobility. Upon introduction of quantum fluctuations, the resonance of "lemniscate" structured operators drive the system into "quantum lemniscate liquid (QLL)" or "quantum lemniscate solid (QLS)". We propose experimental strategies to observe the fractons and discuss the theoretical implications of the QLL/QLS phases.

Introduction – Fractionalization, where the quantum number of low energy excitations is a fraction of the physical constituents (such as electrons), epitomizes strong correlation effects. With reduced phase space amplifying the correlation effects, fractionalization does not require magnetic field in 1D systems [1–5]. However, in higher dimensions, fractionalization has only been confirmed with breaking of time-reversal symmetry either under fractional quantum Hall settings [6, 7] or spontaneous time-reversal symmetry breaking in fractional Chern insulators [8, 9]. Theoretical proposals for fractionalization without time-reversal symmetry breaking have invoked the effects of geometric frustration with local constraints, giving rise to emergent gauge theories in spin models and quantum dimer models [10–19]. More recently, the notion of constraints has been taken to new directions with the advent of fracton models characterized by excitations with restricted mobility [20–26]. While exactly solvable models often offer much theoretical insight [11, 20–23], finding a physical realization of such models has been challenging.

The recent observation of time-reversal invariant incompressible states (i.e., zero Chern number) at fractional filling in twisted bilayer graphene [9] presents a new platform for a strongly correlated state at fractional filling. While the nature of the observed states is still largely unknown, two of us predicted that "fidget spinner"-shaped Wannier orbitals of twisted bilayer graphene can lead to a correlated insulating phase at fractional filling due to the geometric constraints imposed by the shape of the orbitals [27]. While the extensive ground state degeneracy observed in the strong coupling limit [27] implies novel geometrical frustration effects in widely available physical platform, little is known about the nature of excitations and effects of quantum fluctuations. In this paper we evince the fractionalization of doped holes and fractonic nature of the fractionally charged excitations in the strong coupling limit. Furthermore, we derive a resonance in the lemniscate configuration of Wannier orbitals to be the leading quantum fluctuation effect that can result in a QLL/QLS (quantum lemniscate liquid/solid) phase. We explore the properties of the low energy excitations in the QLL/QLS phase and discuss experimental prospects of detecting the proposed fractionalization.

The Model – The topological obstruction forbids symmetric lattice description of the flat bands of magic angle twisted bilayer graphene [28–35]. However, the common alignment of twisted bilayer graphene with hexagonal boron nitride (hBN) explicitly breaks the C_2 rotational symmetry and justifies construction of Wannier orbitals. Nevertheless, the resulting maximally localized Wannier orbitals are extended beyond their AB/BA site centers [29, 36] to the three nearest AA sites, with most of the weight equally divided among the three AA sites, forming a "fidget-spinner" shape (see Figure 1(a)). Consequently, the dominant interaction term is an on-site repulsive interaction projected to the Wannier orbitals taking a "cluster-charging" form [29, 37],

$$H_U = \frac{U}{2} \sum_r \left(\sum_{i \in \hexagon_r} n_i \right)^2 , \tag{1}$$

where $\hexagon_r$ labels the sites belonging to the r-th hexagonal

plaquette and n_i is summed over spin and valley degrees of freedom.

We note that the convention in the literature is to view the moiré lattice as a triangular lattice with one lattice site per unit cell. On the other hand, the Wannier centers form a honeycomb lattice with two sites per unit cell. Hence the conventional filling of 1/3 electrons or holes for each spin and valley per triangular lattice is equivalent to the filling of 1/6 electrons or holes per hexagonal lattice (see Figure 1(a)). Hereafter, we refer to such filling as 1/3 per moiré unit cell. At such 1/3 total filling for spin and valley d.o.f., the energy can be minimized by having the charge carriers occupying only one of the six possible registries (see Figure 1(b). Having 1/3 charges per moiré unit cell corresponds to $\sum_{i\in\hexagon_r} n_i = 1$ per honeycomb plaquette since one charge is shared by three plaquettes.) As pointed out in Ref. [27], the strong coupling limit (i.e., classical) ground state of Equation 1 is extensively degenerate.

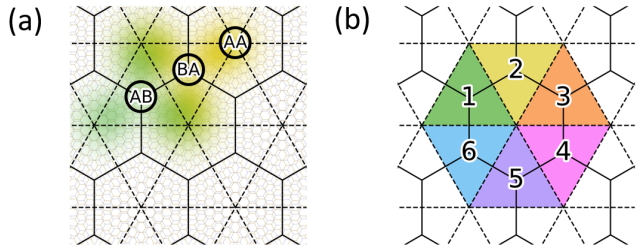

FIG. 1. a) Visualization of Wannier states (WSs), AA, and AB/BA sites in TBG. The light grey lattice denotes a typical moiré pattern formed by a system with a twist angle of 6°. The moiré unit cells formed by the centers of the WSs are delimited by the honeycomb lattice, and its dual triangular lattice is shown in dashed line. The yellow and green blobs schematically represent the shape of Wannier orbitals on the BA and AB sublattices, respectively, with two overlapping charge lobes. For each AB/BA site, there are four orbitals, two from spin and two from valley. (Here the valley d.o.f. is that of the microscopic graphene Brillouin zone, not of the moiré mini Brillouin zone.) (b) Schematic representation of the six-phase registry of AB/BA sites, numbered from 1 to 6 with distinct colors. The vertices of the triangle correspond to the three charge lobes.

Two types of perturbations can lift the extensive ground state degeneracy associated with the cluster-charging interaction of Equation 1: further range interactions and quantum fluctuations. For TBG systems, the Coulomb interaction projected to low energy Wannier orbitals gives rise to various terms including density-density interactions, Hund's coupling, pair-hopping, interaction-mediated hopping, and so on [29, 38, 39]. For the further range interactions, we focus on the 4th nearest neighbor interactions and consider the density-density interactions and Hund's coupling to obtain (See Appendix A for detail.)

$$H_4 = (V_4 - V_4^{approx}) \sum_{\langle ij\rangle_4} n_i n_j - \frac{J_4}{4} \sum_{\langle ij\rangle_4} (S_i^\mu S_j^\mu + n_i n_j), \tag{2}$$

where $n_i = c_{i\alpha}^\dagger c_{i\alpha}$ is the density operator summing over the spin and valley d.o.f. and $S^\mu = c_{i,\alpha}^\dagger T_{\alpha\beta}^\mu c_{j,\beta}$ is the $SU(4)$ spin operator, α, β denote the combined spin-valley d.o.f. with the $SU(4)$ generators $T^\mu \in \{\sigma^\nu, \tau^{\nu'}, \sigma^\nu \otimes \tau^{\nu'}\}$. Following the notation of Ref. [30], V_4 (V_4^{approx}) is the direct Coulomb interaction between 4th nearest neighbor ("point-charge-approximated") Wannier orbitals. The point-charge approximation [30] views the fidget-spinner-shaped Wannier orbitals as being composed of three point charges at AA sites. Focusing on the Eq. (2) is justified by the fact that the difference between the direct Coulomb interaction and the point-charge approximation is short-ranged while all tiling patterns in the ground state manifold of Eq. (1) have the same electrostatic potential under the point-charge approximation. Finally, $J_4 > 0$ is the $SU(4)$ ferromagnetic exchange interaction [38]. Upon introducing quantum fluctuations via hopping term $H_K = \sum_{\langle ij\rangle,\alpha,\tau} t_{ij,\tau}(c_{i,\alpha,\tau}^\dagger c_{j,\alpha,\tau} + h.c.)$ the full Hamiltonian becomes

$$H = H_U + H_4 + H_K. \tag{3}$$

The phase diagram in the strong coupling limit of $t = 0$ was established in Ref. [27]. With finite hopping t, quantum order-by-disorder [40] would select a different quantum ground state, resulting in a qualitative phase diagram we sketch in Figure 2.

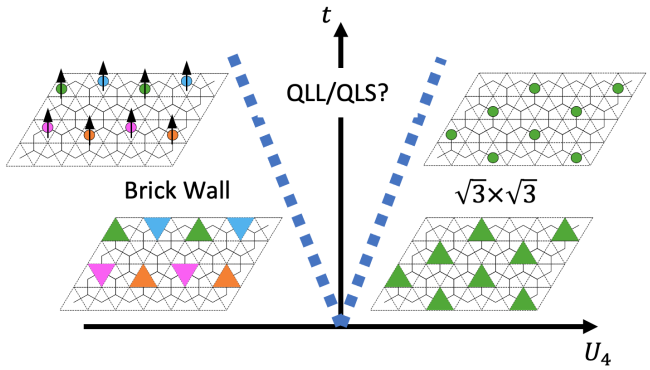

FIG. 2. Proposed phase diagram for the model in Eq. 1. In the strong coupling limit $t = 0$, the ground state is either a brick wall tiling (U_4 negative) or a $\sqrt{3} \times \sqrt{3}$ tiling (U_4 positive). Brick-wall state has SU(4) spin-valley ferromagnetism indicated by black arrows. For both of these phases, we show characteristic tilings, in both triangle and Wannier center representations. Upon increasing t, both states eventually melt "quantum lemniscate liquid" or "quantum lemniscate solid".

Strong Coupling Limit and Fractional Excitations – In the strong coupling limit, the characteristic energy scale

is

$$U_4 = V_4 - V_4^{approx} - \frac{J_4}{2}. \quad (4)$$

For $U_4 < 0$, the system will order into a low-symmetry state dubbed the "brick wall" [27] (Figure 2). The brick wall tiling makes the maximal use of the Hunds coupling to minimize H_4, and will thus be an $SU(4)$ spin-valley ferromagnet. The anisotropic shape of the mesoscale unit results in low symmetry. Translation, mirror and C_3 rotation symmetries of the honeycomb lattice are all broken in the brick wall phase. From the point of view of the Wannier orbital centers (circles in Figure 2), the brick wall state is closely related to the stripe ordered phase proposed in Ref. [38] at filling $n = -3$ of TBG since the brick wall occupies every third sites along a stripe. Hence, the brick wall may be favored at 1/3 filling away from $n = -3$. On the other hand, for $U_4 > 0$, the favored state would be the $\sqrt{3} \times \sqrt{3}$ ordered state, with uniform AB/BA registry. In this case, from Equation 2, configurations with different spin-valley orientations are degenerate within the model. While the two states break translational symmetry in terms of the orbital centers (see filled circles in Figure 2), we anticipate the observable effects of the translational symmetry breaking to be weak due to the spread of the Wannier orbitals. This contrasts the proposed $\sqrt{3} \times \sqrt{3}$ state against the unit-cell tripled charge density wave states proposed in momentum space based numerical approaches [41, 42].

A natural consequence of the incompressible tiling in the strong coupling limit at $\pm 1/3$ filling is the possibility of fractionally charged holes. Intuitively, this can be anticipated by noting that the 1/3 of electron charge is concentrated at the vertices of the dual triangular lattice for any of the incompressible states [30]. By assigning a polarization direction $\vec{P}$ to each of the six phase registries (Figure 3(a)), we can calculate the local charge of a tiling configuration as the bound charge $q_b = \oint d\vec{l} \wedge \vec{P}$. The configuration that binds a 1/3 charge and the energy cost of such an excitation depends on the classical ground state. However, as we show below, their movements are restricted much like fractons and lineons [23, 25, 26].

The $\sqrt{3} \times \sqrt{3}$ phase has two types of charge 1/3 fractional excitations with restricted mobility: vortices (Figure 3(b)) and solitons (Figure 3(c)). As it was previously noted[43], a vortex of phase registry in a charge ordered state usually carries fractional charge. An unusual property of our vortices is their restricted mobility: the cluster charging energy U makes the vortices practically immobile, similar to fractons [23, 24]. However, due to the extensive enegry cost proportional to U_4 associated with the domain walls, the observation of these vortices would require finite temperature. We define a "soliton" of the $\sqrt{3} \times \sqrt{3}$ phase to be the 1/3 charged excitation bound to the end of a line of flipped trimers. In the limit of vanishingly small U_4, a single hole can fractionalize into three solitons which can only move along one dimension associated with the flip line. The soliton dynamics are as if a domain wall state of the Su-Schrieffer-Heeger model[1] were embedded in a two-dimensional space. Hence the soliton behaves like a lineon [23, 24]. However, the solitons in the $\sqrt{3} \times \sqrt{3}$ state are confined. The balance between the flip-line energy cost ($2U_4$ per flip) and the Coulomb interaction between the 1/3 charges determines the size of the bound state (Figure 3(d)). From the estimation of U_4 in Ref.[44], we have $L \sim 1.13 a_M$ (see Appendix B for detailed discussion).

Solitons in the brick wall phase are more intriguing because they are deconfined. First we note that as shown in Figure 3(e), the brick wall phase has sub-extensive ground state degeneracy since each line of "bricks" can choose between two degenerate choices of alternating registries that give different slants to the brick tiling pattern. Hence the ground state degeneracy is 2^L where L is the linear dimension, and the configurational entropy is $L \log 2$. A defect associated with a domain boundary within a row can also be viewed as a "soliton" carrying 1/3 charge (Figure 3(f)) or 2/3 charge (see Appendix B). Similar to the $\sqrt{3} \times \sqrt{3}$ phase, the solitons in the brick-wall phase also have restricted mobility, and can only move along the one dimension of the brick wall rows, which are 2D analogs to the "lineon" excitations in the 3D X-cube model [23, 24]. Furthermore, the solitons in the brick wall phase are deconfined excitations since they cost a finite energy irrespective of the separation between the solitons (see Figure 3(g) and a more detailed illustration in Appendix B.). With the sub-extensive ground state degeneracy and the restricted mobility of the frational-charged quasi-particles, namely "solitons", the brick-wall phase can be viewed as a gapped fracton phase [25, 26, 45].

Quantum Fluctuations – We now turn to the vertical axis of the phase diagram Figure 2 and explore the effects of quantum fluctuations in the limit of $U_4 \ll t$. We ask how the hopping t in H_K would lift the extensive degeneracy of the H_U ground state manifold through quantum "order from disorder" [40]. To start answering this question, we look for an operator that can locally connect two different states in the classical ground state manifold. Such operator should commute with H_U, i.e., keep the cluster charge fixed. Moreover, the operator should act non-trivially in the ground state manifold of H_U at filling $n = \pm 1/3$, without annihilating the states in the manifold. Since the ground state manifold of H_U at filling $n = \pm 1/3$ consists of states with exactly one site of the hexagonal cluster occupied, connecting such states requires coordinated multi-site hopping. We now show that the smallest such operator consists of an eight-site hopping arranged in a *lemniscate*, or sideways figure-eight shape (see Figure 4(c))).

The lemniscate operator $\mathcal{L}_2$ is constructed from the intra-hexagon hopping operator $\mathcal{O}_{\hexagon} = c^\dagger_{i_1} c_{i_2} c^\dagger_{i_3} c_{i_4} c^\dagger_{i_5} c_{i_6}$,

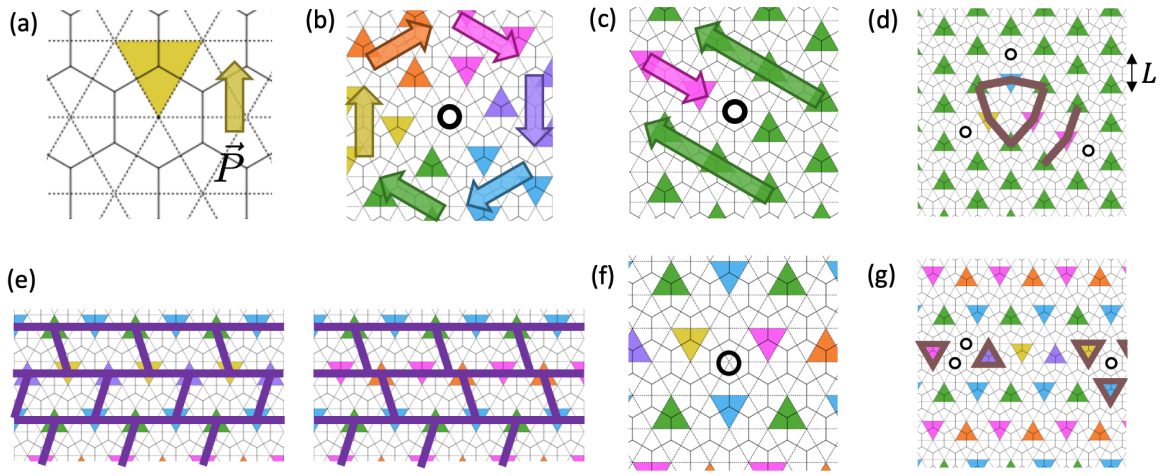

FIG. 3. Catalog of charged excitations in the $t = 0$ phases. a) A single trimer and its associated polarization direction. b) A vortex excitation consists of a single 1/3-charged vacancy (open circle), surrounded by all six registry domains. c) A soliton excitation in the $\sqrt{3} \times \sqrt{3}$ phase consists of a trail with differing registry domain from a uniform background, and d) Three solitons are created from one hole and dessociate. The brown lines indicate the energy cost U_4 associated with the domain walls and L is defined as the linear size of the three-soliton bound state. e) Brick wall state. The sub-extensive degeneracy is indicated by the freedom to flip the second row of the triangles from the configuration in the left panel to the one in the right panel. f) A soliton in the brick wall phase can be thought of as a domain boundary between two degenerate configurations. g) Solitons in the brick wall phase can move along a 1D line with constant energy cost associated with the triangles with brown contour.

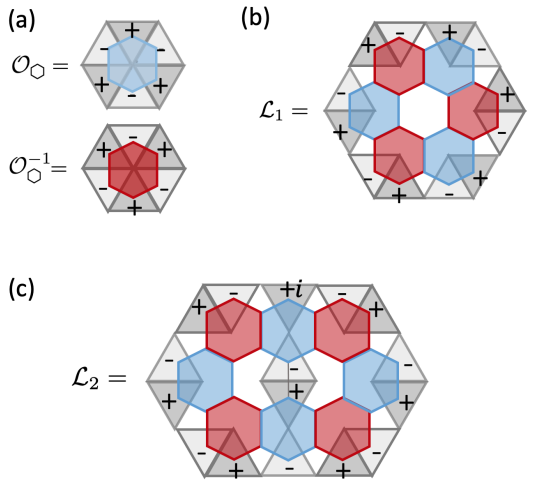

FIG. 4. Visual representation of operators in effective Hamiltonian Equation 5. a) The lowest order term consists of a plaquette operator, in which three sites are acted upon by annihilation operators (-), and the other three by creation operators (+). b) The lowest order operator L_1, which contains only one creation and one annihilation operators on the supported hexagonal plaquettes, spans seven plaquettes, with nontrivial annihilation and creation operators acting on the outermost 12 sites. The middle plaquette must violate the cluster-charging constraint (contain a vortex) given that the surrounding plaquettes satisfy the constraints. c) The lowest order nonvanishing operator L_2 spans 10 plaquettes, where i is a reference site chosen to labeled the position of the operator.

where $i_{1,\ldots,6}$ label the sites belonging to a hexagonal plaquette, organized in a clockwise order (Figure 4(a)). Clearly, $[\mathcal{O}_{\hexagon}, H_U] = 0$, but $\mathcal{O}_{\hexagon}|\psi_0\rangle = 0$ for any $|\psi_0\rangle$ in the ground state manifold of H_U at filling $n = \pm 1/3$ since $\mathcal{O}_{\hexagon}$ annihilates three fermions on a hexagon, but the cluster-charging constraint requires exactly one fermion on each hexagon. However, a larger structure involving multiple hexagons built from alternating $\mathcal{O}_{\hexagon}$ and $\mathcal{O}_{\hexagon}^{-1}$ operators would still commute with H_U and can be made to be compatible with the cluster-charging constraint. A single loop of $\mathcal{O}_{\hexagon}$s and $\mathcal{O}_{\hexagon}^{-1}$s, which we define as $\mathcal{L}_1$ (Figure 4(b)), would only act non-vanishingly on a configuration with a vortex in the center. Hence, the lemniscate operator $\mathcal{L}_2$ illustrated in Figure 4(b) is the smallest operator that can semi-locally resonate between two different states in the classical ground state manifold. There are three orientations of lemniscate operators, related by C_3 rotation. For each orientation, the lemniscate operator connects two local tiling configurations, which we designate as the "flippable" manifold of that operator. Therefore, the low energy effective Hamiltonian can be written as

$$H_{\text{eff}} = H_U - \tilde{t} \sum_{i,\alpha} (\mathcal{L}_{2,i,\alpha} + \mathcal{L}_{2,i,\alpha}^{\dagger}) + H_4 \tag{5}$$

where $\tilde{t} \sim t^8/U^7$, $\alpha \in \{1, 2, 3\}$ label the three different orientations and i labels the position of the operator $\mathcal{L}_2$ (Figure 4(c)).

The effective Hamiltonian H_{eff} is highly frustrated since different $\mathcal{L}_{2,i,\alpha}$'s do not commute. Hence map-

ping out the full quantum phase diagram would require a serious computational effort. Nevertheless, analogies to the quantum dimer models [46] can offer valuable insights. Specifically, as in quantum dimer models, the quantum fluctuations associated with the lemniscate operators would select a novel quantum liquid state or a solid state as a function of $U_4/\tilde{t}$; we refer to these states as "quantum lemniscate liquid/solid" (QLL/QLS)(Figure 2). Among possible QLS states are a plaquette-like state that has resonance within supercells (Figure 4(a)) and a columnar-like state with fixed configurations within supercells that repeats for $U_4 < 0$ (Figure 4(b)) or alternates for $U_4 > 0$. Both the plaquette-like and columnar-like QLS states break C_3 rotational symmetry in addition to the lattice translation symmetry. Despite the reduced symmetry, the emergence of the supercells driven by quantum fluctuations represented by the lemniscate operator sets the QLS states apart from a conventional stripe state. The supercells act as an emergent local degrees of freedom analogous to the emergent orbitals in the so-called cluster Mott insulators on the kagome lattice [47]. However, the emergent orbitals on the kagome lattice are pinned to the honeycomb plaquettes of the lattice, while the supercells form an emergent superstructure in the QLS.

Doping away from 1/3-filling, holes added to the proposed QLS phases can fractionalize into 1/3-charged excitations. However, as in the $\sqrt{3} \times \sqrt{3}$ ordered phase, movements of these 1/3-charged excitations necessarily disrupt"flippable" configurations defining the supercells that are rigidly arranged in the QLS phase(Figure 4(c-d)). Nonetheless, a cooperation between lemniscate resonance and melting of the rigid arrangement of the supercells can lead to deconfinement of the 1/3-charge, which would be a mechanism to quantum melt a QLS state and restore the translational symmetry. Hence, the resulting state at finite doping could be a non-Fermi liquid with 1/3-charged quasi-particles.

Different mechanisms would favor QLL state over QLS at $n = 1/3$, where QLL state is defined by translational symmetry. If such QLL state is gapped, we anticipate deconfined charge 1/3 excitations [48]. Firstly, with the addition of a potential energy term associated with the "flippable" configurations of the lemniscate operator, we anticipate a QLL state at the so-called Rocksar-Kivelson point [11]. Such QLL could either be gapped [15] or gapless [11] but it would be isotropic. Secondly, the resonances unconstrained to a rigid cell (e.g. the dotted hexagon in Figure 5 (b)) could also lead to the melting of QLS to a QLL state. The minimal effective model to address this melting mechanism is to only include the leminiscate operators with one orientation, say the ones aligned with Figure 5 (b) in Eq. 5 since there is no resonance along the other two orientations. (See Appendix C.) The resulting QLL would necessarily break the C_3 rotational symmetry.

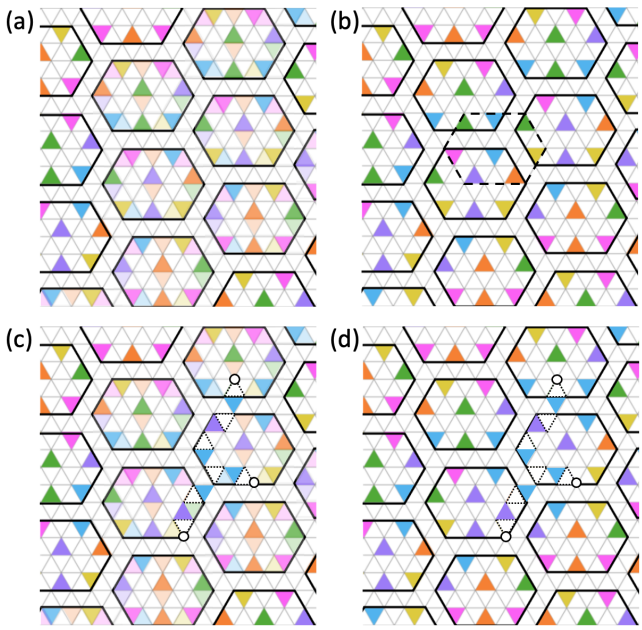

FIG. 5. Cartoon picture of candidate states for QLS. (a) Plaquette-like order, where the resonance happens between the darker shaded triangles and lighter shaded ones. (b) Columnar-like order. The dotted hexagon denotes an extra flippable pattern when the surrounding three states are all aligned. Typical configurations of three fractionalized charge excitations are illustrated in (c) and (d) for plaquette-like order and columnar-like order respectively. The dotted triangles denote the originally occupied sites and the black circles denote the 1/3-charged excitations.

Experimental Implications – Our rich phase diagram with exotic states in experimentally accessible platform opens door for detection and control of novel states. Since all the states of interest are correlated insulating states with Chern number $C = 0$, transport observation of $C = 0$ insulating state[9, 49] is a necessary condition. Solid phases break various symmetries which can be indicators. (i) All the solid phases have characteristic pattern of the AB/BA registry. Scanning tunneling microscopy on the remote bands[50] could reveal associated chemical potential variations. (ii) The brick wall state is a $SU(4)$ spin-valley ferromagnet. (iii) The $\sqrt{3}\times\sqrt{3}$ phase have ferroelectric polarization. (iv) Fractional charge, especially deconfined lineons in brick wall state, can be detected using scanning single electron transistor[51]. The 1D nature of the lineons will give rise to a van Hove singularity where the density of state will diverge as $1/\sqrt{\delta E}$ away from the lineon energy gap [52]. (v) The brick wall and the QLS phases break C_3 rotational symmetry; hence these phases will couple to strain and linearly polarized light. Given the broken symmetries, applying electric field, magnetic field, or lattice strain control the balance among competing states. Hence the fractional correlated insulating states can serve as platform to explore new cor-

related states and fractionalization. How the proposed quantum ground states should evolve into a Fermi liquid inevitable at large hopping would be among interesting future directions, as such tuning are within an experimental reach [53].

Acknowledgements We thank L. Balents, F. Burnell, O. Vafak, S. Vijay, C.N. Lau, M.W. Bockrath, Z. Bi, C.-M. Jian, Y. You, T. Senthil, R. Nandkishore and M. Hermele for illuminating discussions and helpful comments. DM was supported by the Gordon and Betty Moore Foundation's EPiQS Initiative, Grant GBMF10436. KZ was supported by NSF EAGER OSP#136036 and NSERC. E-AK acknowledges funding through Simons Fellows in Theoretical Physics award number 920665 and by the Ewha Frontier 10-10 Research Grant. Part of this work was performed at the Aspen Center for Physics, which is supported by National Science Foundation grant PHY-160761

[1] W. P. Su, J. R. Schrieffer, and A. J. Heeger, Physical Review Letters **42**, 1698 (1979).
[2] K.-V. Pham, M. Gabay, and P. Lederer, Physical Review B **61**, 16397 (2000).
[3] K.-I. Imura, K.-V. Pham, P. Lederer, and F. Piéchon, Physical Review B **66**, 035313 (2002).
[4] D. Orgad, S. A. Kivelson, E. W. Carlson, V. J. Emery, X. J. Zhou, and Z. X. Shen, Physical Review Letters **86**, 4362 (2001).
[5] H. Steinberg, G. Barak, A. Yacoby, L. N. Pfeiffer, K. W. West, B. I. Halperin, and K. Le Hur, Nature Physics **4**, 116 (2008).
[6] R. B. Laughlin, Physical Review Letters **50**, 1395 (1983).
[7] J. Martin, S. Ilani, B. Verdene, J. Smet, V. Umansky, D. Mahalu, D. Schuh, G. Abstreiter, and A. Yacoby, Science (New York, N.Y.) **305**, 980 (2004).
[8] N. Regnault and B. A. Bernevig, Phys. Rev. X **1**, 021014 (2011).
[9] Y. Xie, A. T. Pierce, J. M. Park, D. E. Parker, E. Khalaf, P. Ledwith, Y. Cao, S. H. Lee, S. Chen, P. R. Forrester, K. Watanabe, T. Taniguchi, A. Vishwanath, P. Jarillo-Herrero, and A. Yacoby, Nature **600**, 439 (2021).
[10] P. W. Anderson, science **235**, 1196 (1987).
[11] D. S. Rokhsar and S. A. Kivelson, Phys. Rev. Lett. **61**, 2376 (1988).
[12] I. Affleck and J. B. Marston, Phys. Rev. B **37**, 3774 (1988).
[13] N. Read and S. Sachdev, Physical review letters **66**, 1773 (1991).
[14] X. G. Wen, Phys. Rev. B **44**, 2664 (1991).
[15] R. Moessner and S. L. Sondhi, Physical Review Letters **86**, 1881 (2001).
[16] T. Senthil and M. P. A. Fisher, Phys. Rev. B **62**, 7850 (2000).
[17] A. Kitaev, Annals of Physics **303**, 2 (2003).
[18] A. Kitaev, Annals of Physics **321**, 2 (2006).
[19] C. Castelnovo, R. Moessner, and S. L. Sondhi, Nature **451**, 42 (2008).
[20] C. Chamon, Physical review letters **94**, 040402 (2005).
[21] J. Haah, Phys. Rev. A **83**, 042330 (2011).
[22] B. Yoshida, Phys. Rev. B **88**, 125122 (2013).
[23] S. Vijay, J. Haah, and L. Fu, Phys. Rev. B **92**, 235136 (2015).
[24] S. Vijay, J. Haah, and L. Fu, Phys. Rev. B **94**, 235157 (2016).
[25] R. M. Nandkishore and M. Hermele, Annu. Rev. Condens. Matter Phys. **10**, 295 (2019), arXiv:1803.11196 [cond-mat, physics:hep-th, physics:quant-ph].
[26] M. Pretko, X. Chen, and Y. You, Int. J. Mod. Phys. A **35**, 2030003 (2020), arXiv:2001.01722 [cond-mat, physics:hep-th, physics:quant-ph].
[27] K. Zhang, Y. Zhang, L. Fu, and E.-A. Kim, Communications Physics **5**, 250 (2022).
[28] L. Zou, H. C. Po, A. Vishwanath, and T. Senthil, Phys. Rev. B **98**, 085435 (2018).
[29] H. C. Po, L. Zou, A. Vishwanath, and T. Senthil, Phys. Rev. X **8**, 031089 (2018).
[30] M. Koshino, N. F. Q. Yuan, T. Koretsune, M. Ochi, K. Kuroki, and L. Fu, Phys. Rev. X **8**, 031087 (2018).
[31] J. Kang and O. Vafek, Phys. Rev. X **8**, 031088 (2018).
[32] J. Ahn, S. Park, and B.-J. Yang, Phys. Rev. X **9**, 021013 (2019).
[33] Z. Song, Z. Wang, W. Shi, G. Li, C. Fang, and B. A. Bernevig, Phys. Rev. Lett. **123**, 036401 (2019).
[34] J. Liu, J. Liu, and X. Dai, Phys. Rev. B **99**, 155415 (2019).
[35] Z.-D. Song, B. Lian, N. Regnault, and B. A. Bernevig, Phys. Rev. B **103**, 205412 (2021).
[36] N. F. Q. Yuan and L. Fu, Phys. Rev. B **98**, 045103 (2018).
[37] O. I. Motrunich and T. Senthil, Phys. Rev. Lett. **89**, 277004 (2002).
[38] J. Kang and O. Vafek, Phys. Rev. Lett. **122**, 246401 (2019).
[39] Y.-H. Zhang, D. Mao, and T. Senthil, Phys. Rev. Research **1**, 033126 (2019).
[40] C. L. Henley, Phys. Rev. Lett. **62**, 2056 (1989).
[41] P. Wilhelm, T. C. Lang, and A. M. Läuchli, Physical Review B **103**, 125406 (2021).
[42] S. Zhang, X. Lu, and J. Liu, Physical Review Letters **128**, 247402 (2022).
[43] L. Balents, L. Bartosch, A. Burkov, S. Sachdev, and K. Sengupta, Phys. Rev. B **71**, 144508 (2005).
[44] M. Koshino, N. F. Q. Yuan, T. Koretsune, M. Ochi, K. Kuroki, and L. Fu, Phys. Rev. X **8**, 031087 (2018).
[45] A. Gromov and L. Radzihovsky, Fracton Matter (2022), arXiv:2211.05130 [cond-mat, physics:hep-th].
[46] R. Moessner, S. L. Sondhi, and P. Chandra, Phys. Rev. B **64**, 144416 (2001).
[47] G. Chen and P. A. Lee, Physical Review B **97**, 035124 (2018).
[48] M. Cheng, M. Zaletel, M. Barkeshli, A. Vishwanath, and P. Bonderson, Physical Review X **6**, 041068 (2016), arXiv:1511.02263 [cond-mat, physics:quant-ph].
[49] H. Tian, E. Codecido, K. Zhang, D. Mao, E.-A. Kim, M. Bockrath, and C. Lau, unpublished.
[50] D. Wong, K. P. Nuckolls, M. Oh, B. Lian, Y. Xie, S. Jeon, K. Watanabe, T. Taniguchi, B. A. Bernevig, and A. Yazdani, Nature **582**, 198 (2020).
[51] V. Venkatachalam, A. Yacoby, L. Pfeiffer, and K. West, Nature **469**, 185 (2011).
[52] R. M. Nandkishore, W. Choi, and Y. B. Kim, Physical Review Research **3**, 013254 (2021).
[53] Q. Li, B. Cheng, M. Chen, B. Xie, Y. Xie, P. Wang,

F. Chen, Z. Liu, K. Watanabe, T. Taniguchi, *et al.*, Nature **609**, 479 (2022).
[54] P. P. Ewald, Annalen der Physik **369**, 253 (1921).

Appendix A: Contributions to 4th nearest neighbor density-density interaction

We first describe the direct interaction term. The total electrostatic potential can be written as $V = \sum_{m=4}^{\infty}\sum_{\langle ij\rangle_m} V_m \hat{n}_i\hat{n}_j$, where V_m is the direct Coulomb interaction between the mth nearest neighbor Wannier orbitals. The sum starts at $m = 4$ as the no-touching constraint forbids smaller m. Similar to the Ewald summation [54], we split the electrostatic potential V into a short-range part and a long-range part,

$$\begin{aligned} V &= \sum_{m=4}^{\infty}\sum_{\langle ij\rangle_m}(V_m - V_m^{approx})\hat{n}_i\hat{n}_j + \sum_{m=4}^{\infty}\sum_{\langle ij\rangle_m} V_m^{approx}\hat{n}_i\hat{n}_j \\ &\equiv V_{short} + V_{long}, \end{aligned} \tag{6}$$

where V_m^{approx} is the Coulomb interaction between the mth-nearest neighbor "point-charge-approximated" Wannier orbitals. The point-charge approximation [30] views the fidget-spinner-shaped Wannier orbitals as three point-charges at AA sites. As a result, configurations satisfying the cluster-charging condition have the same electrostatic potential, so V_{long} is a constant. Therefore, we only need to consider V_{short}. Since $V_m - V_m^{approx}$ decays quickly with increasing m [30], we only keep the leading order contribution, which is $m = 4$.

Other than the direct Coulomb interaction, we also take into account the exchange interaction. From the projection of the Coulomb interaction onto the Wannier basis, the exchange term can be written as

$$H_{exchange} = \sum_{i\neq j,\alpha,\beta,\tau,\tau'} J_{ij}^{\tau\tau'} c^{\dagger}_{i,\alpha,\tau}c_{j,\alpha,\tau}c^{\dagger}_{j,\beta,\tau'}c_{i,\beta,\tau'}, \tag{7}$$

where i, j represent Wannier centers, $\alpha, \beta \in \{\uparrow, \downarrow\}$ label the spin, $\tau, \tau' \in \{+, -\}$ label the valley and $V_{ij}^{\tau\tau'} = \sum_{r,r'} V(|r-r'|)\psi^*_{i,\tau}(r)\psi_{j,\tau}(r)\psi^*_{j,\tau'}(r')\psi_{i,\tau'}(r')$ with $V(r-r')$ being the Coulomb potential and $\psi_{i,\tau}(r)$ being the Wannier function. We ignore the inter-valley Hund's interaction since it is negligible compared to Equation 7 [44]. We also assume approximate $SU(4)$ symmetry of the spin-valley d.o.f., that is, $J_{ij}^{++} \approx J_{ij}^{--} \approx J_{ij}^{+-} \approx J_{ij}^{-+} \equiv J_{ij}$ [38]. Therefore, the leading order exchange interaction with J_4 being defined as J_{ij} for 4th nearest neighbors i, j is

$$\begin{aligned} &J_4\sum_{\langle i,j\rangle_4} c^{\dagger}_{i,\alpha,\tau}c_{j,\alpha,\tau}c^{\dagger}_{j,\beta,\tau'}c_{i,\beta,\tau'} \\ =&-\frac{J_4}{4}\sum_{\langle i,j\rangle_4} S_i^{\mu}S_j^{\mu} - \frac{1}{4}J_4\sum_{\langle i,j\rangle_4} n_i n_j, \end{aligned} \tag{8}$$

where $S_i^{\mu} = c^{\dagger}_{i,\eta}T^{\mu}_{\eta\eta'}c_{i,\eta'}$ and the repeated indices are summed over. $\eta, \eta' \in \{1, 2, 3, 4\}$ denote the combined spin-valley indices and T^{μ} is the $SU(4)$ generator with $\mu \in \{1, ..., 15\}$, which we choose to be $\{\sigma^{\nu}, \tau^{\nu'}, \sigma^{\nu}\otimes\tau^{\nu'}\}$, where σ^{ν}, $\tau^{\nu'}$ are Pauli matrices. The last equality in Equation 8 follows from the completeness relation of $SU(2)$, that is $\sigma^{\nu}_{\eta_1\eta_2}\sigma^{\nu}_{\eta_3\eta_4} = 2\delta_{\eta_1\eta_4}\delta_{\eta_2\eta_3} - \delta_{\eta_1\eta_2}\delta_{\eta_3\eta_4}$.

Appendix B: Confinement and deconfinement in $\sqrt{3}\times\sqrt{3}$ and brick wall phases

In this section, we describe the restricted mobility of the vortex and soliton in the $\sqrt{3}\times\sqrt{3}$ and brick wall phases and their confinement properties.

Charge 1/3 vortex in $\sqrt{3}\times\sqrt{3}$

Figure 6(a) shows an immobile vortex quasiparticle, marked by the black empty circle. The vortex is surrounded by all six phases of the AB/BA site registry, and has charge 1/3. Attempting to move this quasiparticle to the location marked by the red empty circle, by flipping the trimer indicated by the arrow, would result in a double occupancy shown by the red cross. Any different attempt to move the vortex would also result in a similar double occupancy.

Confined charge 1/3 soliton in $\sqrt{3}\times\sqrt{3}$

A soliton here has charge 1/3 and can move along a one-dimensional line. It is a boundary between two phases of the AB/BA site registry. In Figure 6(b), the mobility direction is shown by the line of flipped pink triangles, and the soliton acts as a boundary between pink and green phases. Attempting to move the soliton outside of this predefined direction (for example, perpendicular to its mobility direction, to the red empty circle) would, as above, result in a double occupancy (red cross). An electron hole with charge 1 would generate three solitons, each of which can move independently. Figure 6(d) shows a single hole and the individual steps taken in moving one of the three 1/3 charges, flipping one triangle at a time. The three solitons move along different axes related by C_3 symmetry, where shown movement is along the upper-left to bottom-right diagonal.

We now discuss confinement of the solitons. Firstly, their movement leaves behind a trail in the background electronic configuration. This can be seen in Figure 8(a) as trails of blue, magenta, or yellow flipped triangles. Each trimer flipped by the movement of a soliton is associated with a short-range energy cost of $2U_4$ per unit length of $\sqrt{3}a_M$(crimson bonds), and since the number of flips increases with the travelled distance of the

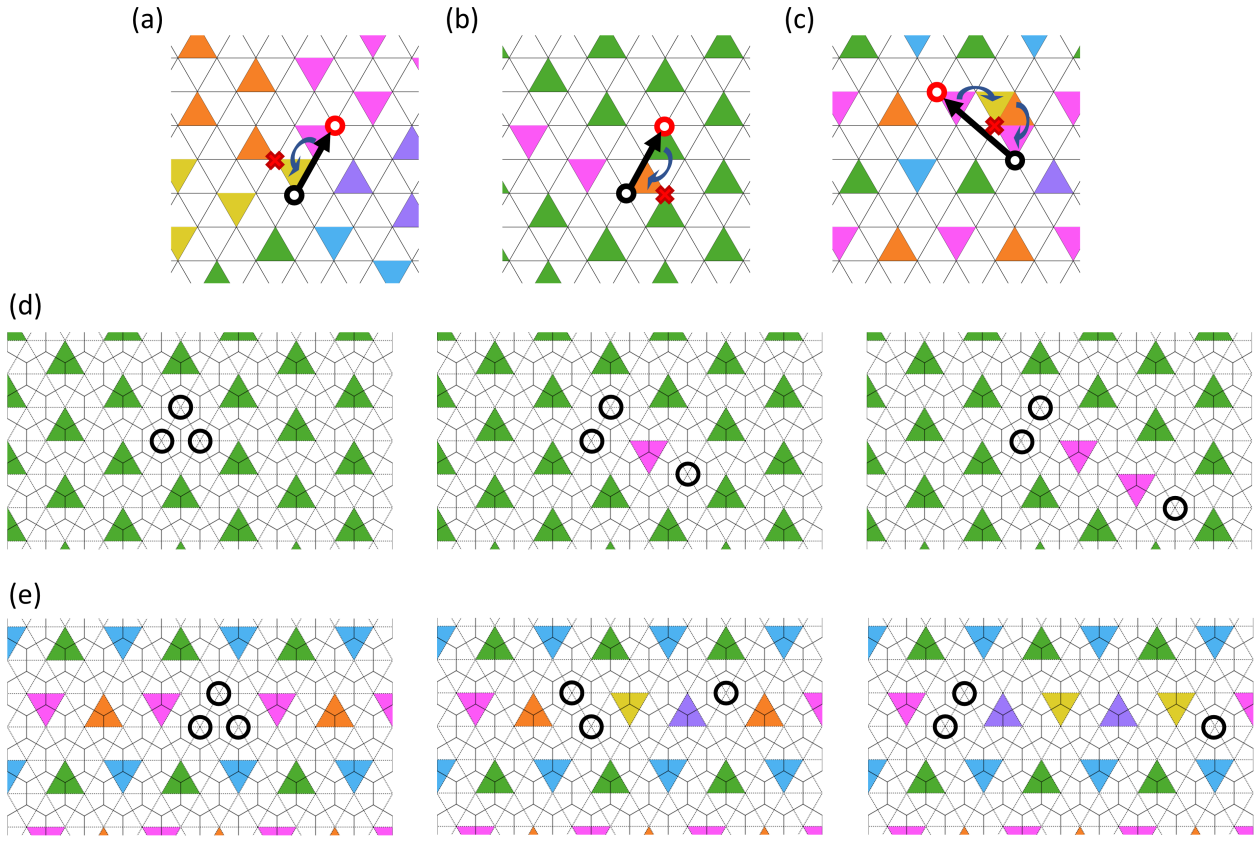

FIG. 6. Restricted mobility of excitations. a) Attempting to move a vortex quasiparticle from the black to red ring by flipping the trimer marked with an arrow would cause a double occupancy shown by the red cross. b) Moving a soliton outside of the allowed direction (upper-left to bottom-right diagonal) in the $\sqrt{3} \times \sqrt{3}$ state would cause a double occupancy. c) Moving a soliton outside of the allowed direction (horizontal) in the brick wall phase requires two flips, but would still cause a double occupancy. d) Soliton movement in the $\sqrt{3} \times \sqrt{3}$ phase. e) Soliton movement in the brick wall phase. The initial hole fractionalizes into a left-moving soliton with charge $2/3$ and a right-moving soliton with charge $1/3$.

solitons, they are confined in this phase. There is also long-range Coulomb repulsion of the charges. Hence, the total energy cost for a three-soliton configuration with linear dimension l is given by $E(l) = 3\left(2U_4\frac{l}{\sqrt{3}a_m}\right) + 3\frac{e^2}{9\epsilon a_m(1+\sqrt{3}l)}$, where ϵ is the dielectric constant and a_M is the moiré lattice constant. By minimizing $E(l)$, we obtain the confinement length L. For the solitons to have finite confinement length, i.e. $L > 0$, $U_4 < \frac{e^2}{6\epsilon a_M}$ must hold. The confinement length is $L = \frac{1}{\sqrt{3}}\left[\sqrt{\frac{a_M e^2}{6\epsilon U_4}} - a_M\right]$.

Deconfined charge $1/3$ and $2/3$ solitons in brick-wall

The brick-wall phase also hosts solitons (Figure 6(e)), but with different mobility and confinement properties. Due to the reduced symmetry of the brick-wall phase, the nature of the solitons is significantly more complex than the $\sqrt{3}\times\sqrt{3}$ case. We first define the soliton by analyzing the constraints on the ground-manifold of the brick-wall state. Without loss of generality, we consider rows of bricks that are horizontally-aligned (Figure 6(f)). In this state, the trimers also form rows of alternating AB/BA (up/down) centers. There are three possible "phases" for the rows: R_1 (cyan/green), R_2 (purple/yellow), and R_3 (magenta/orange). In order to maximize the number of U_4 bonds per trimer, each row must have a phase differing from those of the rows above and below. Two adjacent rows with the same phase would not form any U_4 bonds (Figure 7(c)), and thus be suboptimal in energy. This constraint is the origin of the subextensive entropy of the brick wall state. If one "fills up" the lattice sequentially from top to bottom with rows of trimers, there will always be two allowed phases for each row (Figure 7(a,b)).

A soliton, then, can be viewed as a boundary between two phases within a row (Figure 7(d)). A $1/3$ charge soliton is a boundary between R_1/R_2, or R_2/R_3, or R_3/R_1 (viewed from left to right). Two $1/3$ charge solitons can also join together to form a $2/3$ charge soliton, which is the boundary between R_1/R_3, or R_2/R_1, or R_3/R_2 (again from left to right). The solitons can move horizontally by flipping trimers. However, like earlier, any movement of a soliton outside of the mobility direction would result in a double occupancy (Figure 6(c)). Here, the movement would require two nearest-neighbor flips (denoted by the two arrows). Figure 6(e) shows a single hole, fractionalized into a $2/3$ soliton moving to the left, and a $1/3$ soliton moving to the right. Unlike the $\sqrt{3}\times\sqrt{3}$ phase, all solitons move along the same axis.

Remarkably, the solitons shown in Figure 6(e) are deconfined. Earlier, confinement arose from the solitons' movement leaving behind trails of flipped trimers that cost energy via U_4. Analogously, here we ask the question of whether the solitons' movement costs energy scaling with distance. As established earlier, solitons separate domains of R_1, R_2, or R_3. Fractionalization of a single hole would result in at least two different phases existing within the same row. Therefore, if the rows above and below have differing phases, the solitons would leave behind a trail of flipped trimers that would be in the same phase as one of the rows above or below, and cost an average energy of $|U_4|$ per two flips (unit length of $3a_M/2$). The total energy cost here for a three-soliton configuration where the central $1/3$ charge remains stationary is approximately $E(l) = 2|U_4|\frac{l}{3a_M} + \frac{5}{2}\frac{e^2}{9\epsilon a_M l}$. The confinement length here, obtained by minimizing E, would be $L = \sqrt{\frac{5a_m e^2}{12|U_4|\epsilon}}$.

On the other hand, if the rows above and below the hole have the same phase, there can be two different domains that satisfy the U_4 constraint. This suggests that the hole could fractionalize into a pair of $1/3$ charge and $2/3$ charge solitons that are boundaries between the two allowed phases. Figure 8(b) shows one such case of a hole in a R_1 row, where the rows above and below are R_3. The $2/3$ charge and $1/3$ charge solitons form left and right boundaries respectively for the central region of R_2. In this case, the $2/3$ soliton must be on the left side; if it were on the right, the central domain would be R_3 and therefore not allowed. In general, the direction that the $2/3$ soliton moves in depends on the surrounding domains. Due to Coulomb repulsion, the individual quasiparticles that make up the $2/3$ soliton would separate somewhat, leading to a bound state of two $1/3$ solitons (Figure 8(c)) with length scale $L = \sqrt{\frac{a_M e^2}{6|U_4|\epsilon}}$ obtained by minimizing the energy $E(l) = |U_4|\frac{l}{3a_m/2} + \frac{e^2}{9\epsilon a_M l}$. Still, the $2/3$ charge bound state as a whole is deconfined. Overall, since the energy cost (broken U_4 bonds in Figure 8(b,c)) is localized to a finite area around all of the solitons, they are deconfined.

Appendix C: Effective model for melting QLS

Here we propose a minimal effective model for studying the melting of the QLS proposed in the main text by regarding the supercells of the "flippable" configurations as local degree of freedoms. How these local d.o.f are related to the QLS is illustrated in Figure 9 (a). The effective model is defined on a distorted triangular lattice with four orbitals per unit cell labelled by the four colors in Figure 9 (b). For each site, we define a local three dimensional Hilbert space spanned by $|0\rangle, |1\rangle, |-1\rangle$. The two states $|\pm 1\rangle$ denote the two "flippable" configurations of the lemniscate operator, where $|1\rangle(|-1\rangle)$ denotes the orientation of the middle two triangles being "up"("down")-pointing (Figure 9 (a)). The $|0\rangle$ state denotes an "un-flippable" configuration. By considering the possible resonance within the QLS, we arrive at the minimal effective Hamiltonian that could describe the melting

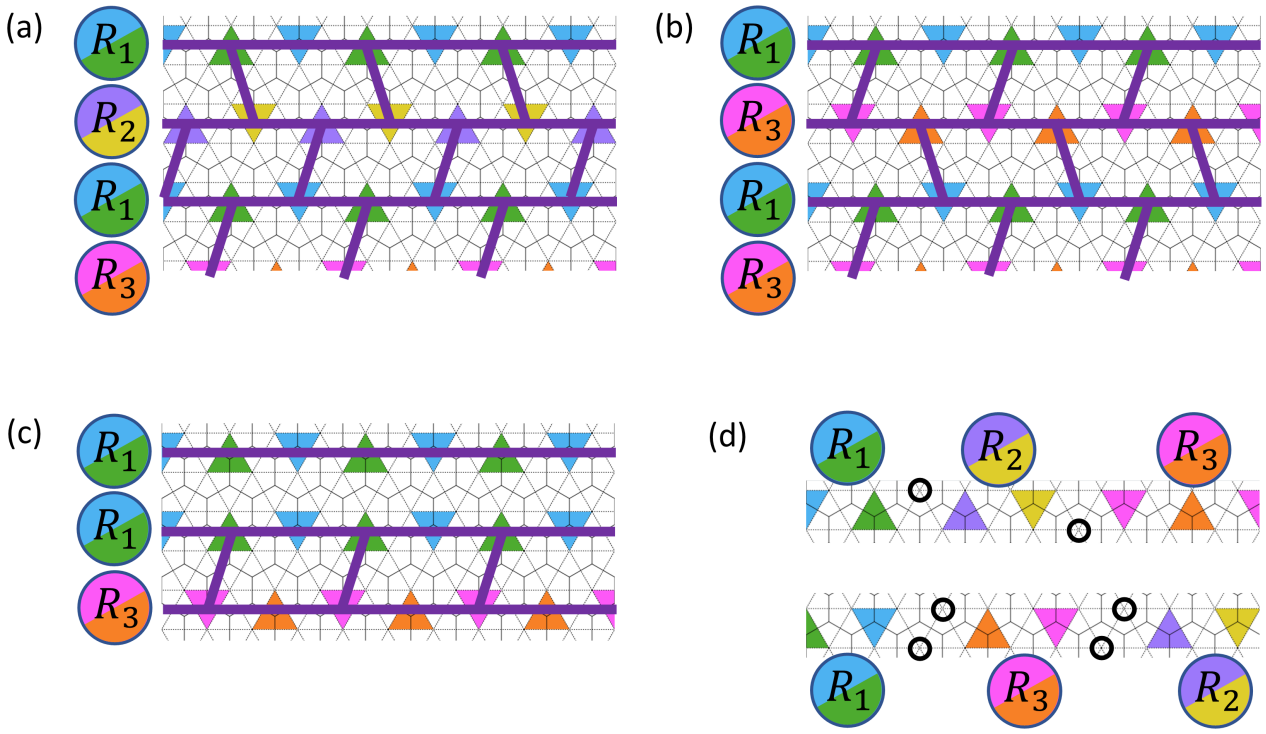

FIG. 7. Three domains of trimer rows in the brick-wall phase. a,b) Each row must have a differing phase from the rows above and below. The residual freedom manifests as sub-extensive entropy, which can be seen through the freedom in choosing "slant directions" for each row of bricks. c) Two adjacent rows with the same phase would not be able to form U_4 bonds, and is thus suboptimal in energy. d) 1/3 charge solitons are domain walls between two of the three phases. Likewise, 2/3 charge solitons are also domain walls, but with the opposite direction of cycling between the three phases.

of QLS to a nearby QLL phase,

$$H_{\text{eff}}^{\text{QLS}} = -J_Q \sum_{\langle i,j\rangle,a} \tau_{i,a}^z \tau_{j,a}^z - \tilde{t}\mathcal{P}\left(\sum_{i,a} \tau_{i,a}^x\right)\mathcal{P}, \qquad (9)$$

where $a \in \{1,2,3,4\}$ labels the orbitals, i,j label the sites, $\tau^{x,y,z}$ are the Pauli matrices acting on $|\pm 1\rangle$ states and $\mathcal{P}$ is a projection operator. $J_Q > 0 (< 0)$ denotes the nearest neighbor FM (AFM) coupling between the same orbitals that favors a QLS state. $\tilde{t}$ denotes the strength of the lemniscate resonance. Without the projector $\mathcal{P}$, the Hamiltonian $H_{\text{eff}}^{\text{QLS}}$ is the same as a transverse field Ising model, whose phase diagram is well-known. Now let us specify the definition of $\mathcal{P}$, which encodes the non-trivial correlation depicted in Figure 9 (a). The projection imposes local constraints such that for each triangle formed by the three nearest neighbor sites with the same colors in Figure 9, if the three sites are all in state $|1\rangle$, the site that is enclosed by the triangle has to be in state $|-1\rangle$ ($|0\rangle$) for right (left)-pointing triangles, similar for the case where all the three sites are in state $|-1\rangle$. The projection $\mathcal{P}$ makes $H_{\text{eff}}^{\text{QLS}}$ non-trivial and whether the ground state of $H_{\text{eff}}^{\text{QLS}}$ could be a spin liquid is an open question.

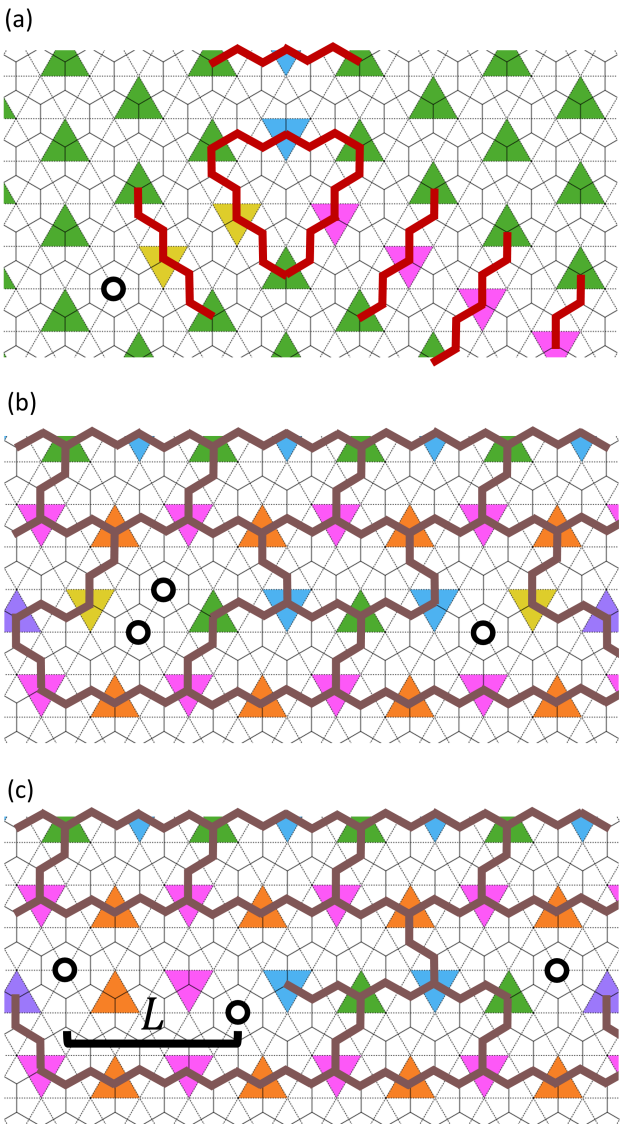

FIG. 8. Confinement cost of solitons in the $t = 0$ phases. a) In the $\sqrt{3} \times \sqrt{3}$ phase, the trail of flipped trimers caused by the movement of a soliton costs an energy of $2U_4$ per unit length (red lines show U_4 bonds which cost energy). b) In the brick wall phase, the trail of flipped trimers is able to form U_4 bonds with the surrounding R_3 phase above and below (brown lines show U_4 bonds which lower the energy). The two solitons enclose a new R_1 domain in the middle of the R_2 phase, both of which satisfy the U_4 constraint. c) The 2/3 charge soliton could separate to form a bound state with finite size L due to Coulomb repulsion, but the bound state remains deconfined.

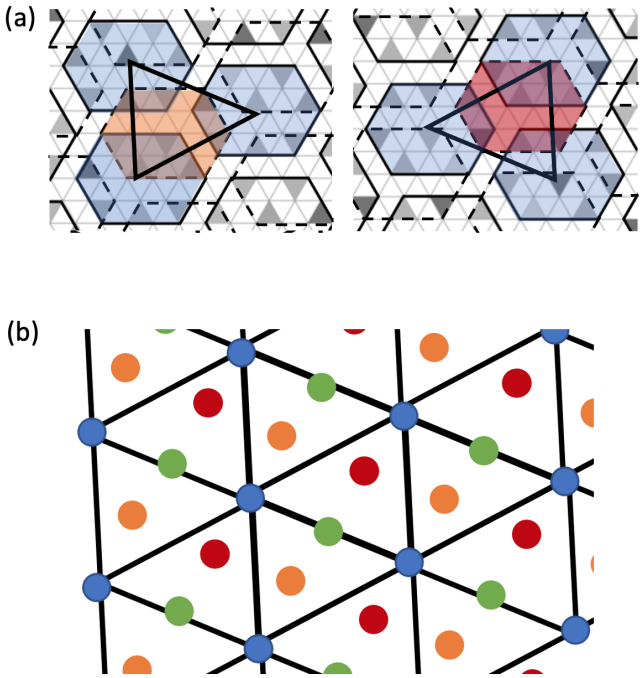

FIG. 9. The resonance in QLS and effective lattice model. a) The additional "flippable" configurations in QLS. Left: an additional "down"-pointing configuration (orange shade) emerges by arranging three "up"-pointing configurations (blue shade) arranged in a right-pointing triangle (thick black lines). Right: an additional "up"-pointing configuration (red shade) emerges by arranging three "down"-pointing configurations (shaded in blue) arranged in a left-pointing triangle (thick black lines). b) The lattice constructed by viewing the centers of the "flippable" configurations in a) (marked by the elongated hexagons) as lattice sites. The blue, orange and red sites correspond to the shaded plaquettes with the same colors in a). (The green sites are not shown explicitly in a).